J. Fluid Mech. (1996), *vol.* 315, *pp.* 1–29

Low Reynolds number fully developed two-dimensional turbulent channel flow with system rotation

By KOICHI NAKABAYASHI AND OSAMI KITOH
Nagoya Institute of Technology, Gokiso-cho, Showa-ku, Nagoya 466, Japan

(Received 18 October 1994 and in revised form 30 October 1995)

Theoretical and experimental studies have been performed on fully developed two-dimensional turbulent channel flows in the low Reynolds number range that are subjected to system rotation. The turbulence is affected by the Coriolis force and the low Reynolds number simultaneously. Using dimensional analysis, the relevant parameters of this flow are found to be Reynolds number $Re^* = u_* D/\nu$ (u_* is the friction velocity, D the channel half-width) and $\Omega\nu/u_*^2$ (Ω is the angular velocity of the channel) for the inner region, and Re^* and $\Omega D/u_*$ for the core region. Employing these parameters, changes of skin friction coefficients and velocity profiles compared to non-rotating flow can be reasonably well understood. A Coriolis region where the Coriolis force effect predominates is shown to exist in addition to conventional regions such as viscous and buffer regions. A flow regime diagram that indicates ranges of these regions as a function of Re^* and $|\Omega|\,\nu/u_*^2$ is given from which the overall flow structure in a rotating channel can be obtained.

Experiments have been made in the range of $56 \leqslant Re^* \leqslant 310$ and $-0.0057 \leqslant \Omega\nu/u_*^2 \leqslant 0.0030$ (these values correspond to $Re = 2U_m D/\nu$ from 1700 to 10000 and rotation number $Ro = 2|\Omega| D/U_m$ up to 0.055; U_m is bulk mean velocity). The characteristic features of velocity profiles and the variation of skin friction coefficients are discussed in relation to the theoretical considerations.

1. Introduction

In engineering, one encounters different kinds of flow through a duct that is rotating around an axis perpendicular to its axis: for example, flows in turbo-machinery or through a cooling passage in a rotating machine such as a gas turbine or electric motor. The flow in a rotating duct undergoes Coriolis force effects. Mean axial velocity U_m, rotation angular velocity Ω and the geometry of the duct (its size and cross-sectional shape) vary widely from flow to flow, and the flow characteristics differ accordingly. The various characteristics of the flow phenomena in a rotating duct are attributed to the combination of two kinds of Coriolis force effects on the flow. First, a secondary flow is induced within a duct if there is a mean vorticity component perpendicular to the rotating axis (caused by the endwall effect). Secondly, there are promoting/suppressing effects on the turbulence if there is a mean vorticity component parallel to the rotating axis. The two effects are exerted simultaneously on flows in a rectangular duct having a small aspect ratio, say of less than four, and the velocity distributions change appreciably from stationary duct flow. Moore (1967) indicated that the secondary flow is a major reason for the change in low-aspect-ratio ducts in the range of his experimental spin parameter. If we confine ourselves to ducts having an aspect ratio larger than four and consider the flow only in a mid-plane of the duct, the secondary flow caused by the endwall effect does not appear and the flow can be seen as nominally two-dimensional. The Coriolis force has only the *latter* effect on the two-dimensional flow. On the suction side of the channel, the turbulent activities are weakened, whereas they are augmented on the pressure side, and the velocity distributions across the channel deform accordingly.

Pioneering work was done by Johnston, Haleen & Lezius (1972) on the fully developed turbulent flow through a duct of aspect ratio seven. They measured the velocity distributions at the rather high Reynolds number range of $11\,500 \leqslant Re \leqslant 35\,000$ and the rotation number Ro up to 0.21. Here the Reynolds number Re and the rotation number Ro are defined based on bulk mean velocity U_m and channel height $2D$ as $Re = 2U_m D/\nu$, $Ro = 2|\Omega| D/U_m$. Together with the results obtained by flow visualization, they demonstrated the Coriolis effect in three stability-related phenomena: (i) it changes the wall-layer streak bursting rate which causes the modification of turbulent energy and mean velocity profile; (ii) it can suppress the transition to turbulence in the suction-side flow; (iii) it may develop a large-scale roll cell in the pressure-side flow. An appropriate local stability parameter is shown to be the Richardson number that was introduced by Bradshaw (1969) for the rotating flow by analogy with stratified flow.

Launder, Tselepidakis & Younis (1987) made a numerical calculation for fully developed rotating channel flow using second-moment closure and obtained good agreement with the experimental results of Johnston *et al.* Shima (1993) used an improved second-moment closure to simulate the flow that can be applicable when including relaminarization phenomena. Both simulations succeeded somewhat in capturing the Coriolis force effects on the velocity and turbulence intensity distributions because, unlike the k–ϵ model, the second-moment closure includes explicitly the Coriolis force terms which have a crucial role in changing the structure of turbulence. Large-eddy simulations (LES) were made by Miyake & Kajishima (1986) and by Kim (1983) up to rotation numbers 0.2 and 0.068, respectively. Miyake & Kajishima presented various statistical turbulence quantities and concluded that near the wall the Coriolis force enhances sweep and ejection on the pressure side, while reducing them on the suction side. Kristoffersen & Andersson (1993) recently performed DNS at Reynolds number $Re = 5800$ and rotation number up to 0.5. They showed that relaminarization occurs on the suction side, and Taylor–Görtler-like counter-rotating streamwise vortices appear on the pressure side if the rotation number is sufficiently high.

When the Reynolds number is low, a rotating channel flow is subjected to the Reynolds number effect in addition to the Coriolis force effect. It is known that the low Reynolds number flow is apt to be more strongly affected by Coriolis force effects than the high Reynolds number flow. In practice there exist low Reynolds number flows such as a rotating machine cooling passage the dimension of which must be small owing to a geometrical constraint. Thus, from an engineering point of view, it is also necessary to understand Coriolis force effects in the low Reynolds number range. The main objective of the present work is to elucidate the overall flow structure that is simultaneously affected by the Coriolis parameter and Reynolds number effects.

In §2 the control parameters and velocity similarity formulae are developed from dimensional considerations. The experimental apparatus and methods are given in §3. In §4 the experimental results and discussion, first for non-rotating low Reynolds number flow then for rotating channel flow, are presented. Finally, some concluding remarks are given in §5.

2. Theoretical considerations

2.1. *Dimensional analysis*

Here we consider turbulent flow through a two-dimensional channel that is rotating with angular velocity Ω around the z-axis, (figure 1). The flow is in the x-direction and fully developed so that the mean velocity U changes in the y (wall distance) direction only. The configurations of the pressure and suction sides in figure 1 are reversed when $\Omega < 0$. The channel width is $2D$. The velocity U is described as a function of five variables:

$$U = f_1(D, y, u_*, \nu, \Omega), \tag{1}$$

where u_* and ν are friction velocity and kinematic viscosity, respectively, and are conveniently set to make (1) non-dimensional for the flow close to the wall. The non-dimensional velocity can then be written as

$$U/u_* = f_2(yu_*/\nu,\ u_*^2/\Omega\nu,\ u_* D/\nu). \tag{2}$$

The corresponding functional relation holds for the velocity gradient:

$$\mathrm{d}(U/u_*)/\mathrm{d}(yu_*/\nu) = f_3(yu_*/\nu,\ u_*^2/\Omega\nu, u_* D/\nu). \tag{3}$$

These equations show that the non-dimensional mean velocity and its gradient normalized by u_* and ν/u_* are functions of the distance from the wall $y^+ = yu_*/\nu$, the Coriolis parameter $\Omega\nu/u_*^2$, and the Reynolds number $Re^* = u_* D/\nu$.

Three length scales appearing in the present turbulent flow are the viscous δ_v and Coriolis δ_c lengths and channel half-width D. The viscous length scale $\delta_v(= \nu/u_*)$ is a measure of the distance from the wall within which the viscous effect on the flow predominates. The Coriolis length scale $\delta_c(= u_*/|\Omega|)$ is a measure of the distance from the wall above which the Coriolis force plays an important role. D is a measure of the largest length scale (or other length scale) of the flow. Using these length scales, three independent variables in (2) and (3) can be expressed as ratios among these scales and y. The alternative expression for (2) then becomes

$$U^+ = U/u_* = f_2(y/\delta_v,\ \pm\delta_c/\delta_v, D/\delta_v), \tag{4}$$

where the plus or minus sign indicates pressure or suction side, respectively. In the case of non-rotating channel flow having high Reynolds number, the last two parameters in (4), δ_c/δ_v and D/δ_v, are no longer necessary to describe the flow, for $\delta_c/\delta_v = \infty$ and D/δ_v is significantly large. Then (4) reduces to the well-known wall law

$$U^+ = f_4(y^+). \tag{5}$$

2.2. *Flow regime of rotating channel flow*

Flows within a rotating channel are characterized by two parameters, $\pm\delta_c/\delta_v$ and D/δ_v, which are ratios among the three length scales δ_v, δ_c and D. These scales play a significant role in the regions

$$y < K_1\delta_v \quad \text{(viscous length scale } \delta_v\text{)}, \tag{6a}$$

$$y > K_2\delta_c \quad \text{(Coriolis length scale } \delta_c\text{)}, \tag{6b}$$

$$y > K_3 D \quad \text{(outer length scale } D\text{)}, \tag{6c}$$

where K_1, K_2 and K_3 are constants. Figure 2 schematically shows the flow field divided into several areas, in which the particular length scales prevail. The boundaries between the areas can be drawn on a $(|\Omega|\,\nu/u_*^2, Re^*)$ parameter plane as in figure 3. We call this

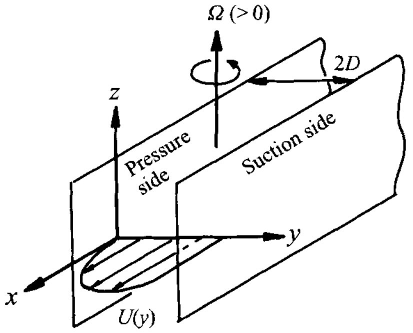

FIGURE 1. Flow geometry and coordinate system. Pressure and suction sides in the figure are for $\Omega > 0$.

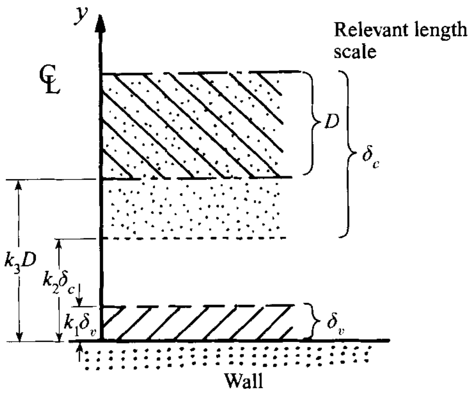

FIGURE 2. Ranges of each length scale.

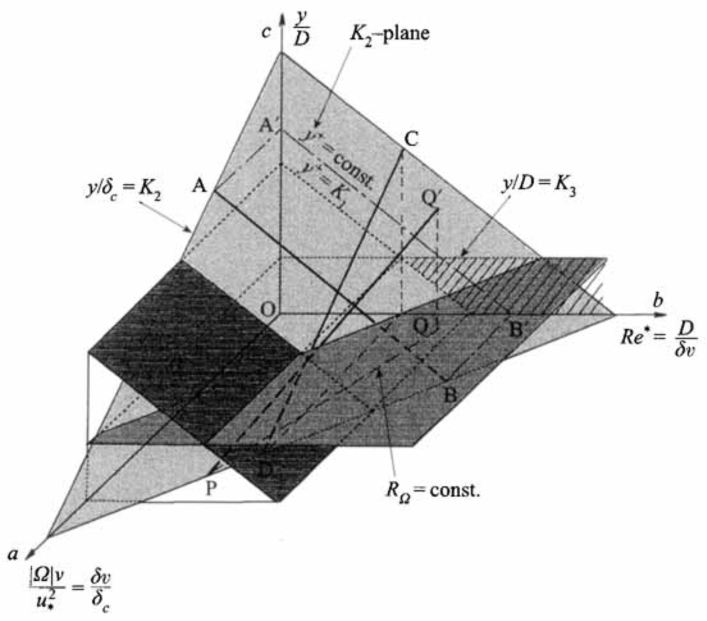

FIGURE 3. Flow regime diagram.

a flow regime diagram because each area enclosed by the boundaries has its own flow characteristics. This diagram indicates geometrically how the flow structure changes as the parameters Re^* and $|\Omega|\nu/u_*^2$ vary.

The axes a and b of the diagram indicate the Coriolis parameter $|\Omega|\nu/u_*^2$ and Reynolds number Re^* in a log scale, respectively. Plane bOc perpendicular to the a-axis shows the flows that are substantially unaffected by the Coriolis force (extremely small $|\Omega|\nu/u_*^2$). The line parallel to the b-axis ($y/D = K_3$) indicates a boundary above which the flow is influenced by the scale D. The broken line ($y^+ = K_1$) is the upper boundary of the viscosity-affected region. From much experimental data on channel flow, the constants K_1 and K_3 are seen to have values of around 30–50 and 0.2–0.3, respectively. As Re^* increases, a region appears that is bounded above and below by these two lines (hatched area) where neither D nor δ_v influences the flow and the velocity follows a log law.

The plane aOc perpendicular to the b-axis shows flows having a constant Reynolds number, low Re^*. The line $y/\delta_c = K_2$ is the lower boundary of the region where the Coriolis force has an appreciable effect on the flow. In the diagram a surface satisfying the relation $y/\delta_c = K_2$ is given by the equation

$$\ln(y/D)+\ln(\delta_v/\delta_c) = \ln(K_2)-\ln(Re^*). \tag{7}$$

This surface, called the K_2-plane hereafter, is the lower boundary of the region affected by the Coriolis force.

When the flow Re^* is increased but $|\Omega|\nu/u_*^2$ is kept constant, the lower boundary of the Coriolis-force-affected region is shown, say, by the bold line A–B on the K_2-plane. This line has a constant value of y^+, as can be seen when it is projected on the bOc-plane as the fine chain line A′–B′. On the other hand, when $|\Omega|\nu/u_*^2$ is increased but Re^* is kept constant, the lower boundary is shown by the bold line C–D on the K_2-plane. The line projected on the bOc-plane shows that the Coriolis force effect penetrates deep into smaller y^+ as $|\Omega|\nu/u_*^2$ is increased. This means that the lower boundary, if expressed by a wall variable, depends only on $|\Omega|\nu/u_*^2$, and not on Re^*. The value of K_2 is not yet known but has a value of the order of 10^{-3} as shown later from experimental data.

Jacquin *et al.* (1990) developed a similar consideration of the interaction between the Coriolis length $l_c (= v'/2\Omega, v'$ is turbulence intensity) and the integral scale of turbulence L for homogeneous turbulent flow within a rotating frame. Using the ratio between these two length scales l_c/L, the Rossby number, they discussed the dissipation rate of the turbulence in a rotating frame. They also considered the viscous effects as well by using a parametric diagram among Ekman, Rossby and Reynolds numbers.

2.3. *Similarity laws of the velocity profile*

Figure 3 indicates that the flow in a rotating channel can be divided into several different regions where particular length scales dominate. In each region a velocity similarity law is expected to exist.

2.3.1. *Viscous and buffer region*

Very close to the wall, where $y/\delta_v = y^+$ is less than K_1, the viscous length scale plays an important role and equation (3) can be expanded as

$$\mathrm{d}(U/u_*)/\mathrm{d}(y/\delta_v) = 1+A_1y^+ + A_2y^{+^2}\dots, \tag{8}$$

where $A_1, A_2, \dots$, are constants. A well-known velocity profile $U^+ = y^+$ results from (8) for extremely small y^+, usually $y^+ < 5$. Various functional relations are proposed for a slightly higher value of y^+. Among them, the Van-Driest formula is the most useful, for it can apply beyond the buffer region as well. This formula,

$$U^+ = \int_0^{y^+} \frac{2\,\mathrm{d}y^+}{1+[1+4\kappa^2 y^{+^2}\{1-\exp(-y^+/A^+)\}^2]^{1/2}} \tag{9}$$

includes two constants, A^+ and κ. A^+ is the Van-Driest damping factor and κ the Kármán constant. If the Reynolds number is very high and $|\Omega|\,\nu/u_*^2$ is small, A^+ is 26 and $\kappa = 0.4$.

When Re^* is small and/or $|\Omega|\,\nu/u_*^2$ is large and satisfy the following relations;

$$Re^* < K_1/K_3, \tag{10}$$

$$|\Omega|\,\nu/u_*^2 > K_2/K_1, \tag{11}$$

the effects of scale D and/or δ_c appear in the buffer or viscous region. Under these conditions, the coefficients $A_1, A_2, \ldots$ in (8) and A^+ and κ in (9) are no longer constant but depend on Re^* and/or on $\Omega\nu/u_*^2$ like

$$A_i = A_i(Re^*, \Omega\nu/u_*^2), \quad i = 1,2,\ldots, \tag{12}$$

$$A^+ = A^+(Re^*, \Omega\nu/u_*^2), \quad \kappa = \kappa(Re^*, \Omega\nu/u_*^2). \tag{13}$$

2.3.2. *Log and Coriolis regions*

In the log region that appears in high Reynolds number flow, no characteristic length scales prevail. Re^* should be larger than K_1/K_3 for the log region to exist in a stationary channel. Equation (3) then reduces to the simple relation

$$\mathrm{d}(U/u_*)/\mathrm{d}(y/\delta_v) = 1/(\kappa y/\delta_v) \tag{14}$$

which gives a well-known log-law:

$$U^+ = (1/\kappa)\ln y^+ + C_1. \tag{15}$$

In figure 3, the shaded area on the *bOc*-plane corresponds to this region. In a rotating channel, an additional condition $K_1\,\delta_v < K_2\,\delta_c$ is necessary for the log region to exist so that the Coriolis force effect does not appear there.

The log region is penetrated by the Coriolis length scale if $|\Omega|$ is increased and the relation

$$K_3\,D > K_2\,\delta_c \tag{16}$$

holds. In the penetrated region, δ_c is the only length scale of the flow, and equation (3) can be expanded like

$$\frac{\mathrm{d}U^+}{\mathrm{d}y^+} = \frac{1}{\kappa y^+} - 2\beta\frac{\Omega\nu}{u_*^2} \tag{17}$$

so that $\mathrm{d}U/\mathrm{d}y$ depends on δ_c and u_* but not on δ_v and D. Here, 2β is a constant. Integrating this with y^+, we obtain the velocity formula

$$U^+ = \frac{1}{\kappa}\ln y^+ - 2\beta\frac{\Omega\nu}{u_*^2}y^+ + C_2, \tag{18}$$

where C_2 is an integral constant. This relation is consistent with the one developed by Bradshaw (1969) for the flow affected by the Coriolis force using the Monin–Oboukov formula. The constant β is called the Monin–Oboukov coefficient. Subtracting (15) from (18) gives the velocity difference ΔU^+ from the conventional log law as

$$\Delta U^+ = -2\beta\frac{\Omega\nu}{u_*^2}y^+ + (C_2 - C_1). \tag{19}$$

Here, if we introduce a new variable, $y_c^* = y/\delta_c$, an alternative similarity expression for the velocity gradient can be obtained:

$$\mathrm{d}U^+/\mathrm{d}y_c^* = f_5(y/\delta_c). \tag{20}$$

The region where the above relation holds is called the Coriolis region, for only the Coriolis length scale plays a role there. Integrating (20) with respect to y_c^*, we obtain

$$U^+(y_c^*) - U^+(y_{c0}^*) = \int_{y_{c0}^*}^{y_c^*} f_5(y_c^*)\,\mathrm{d}y_c^* = F_5(y_c^*) - F_5(y_{c0}^*), \tag{21}$$

where y_{c0}^* is the lowest value of y_c^* in the Coriolis region. A comparison of equations (18) and (21) shows that $F_5(y_c^*)$ has the following form:

$$F_5 f_5(y_c^*) = \frac{1}{\kappa}\ln y_c^* \pm 2\beta y_c^*, \tag{22}$$

where plus and minus signs correspond to the suction and pressure sides, respectively. Thus f_5 is expressed as

$$f_5(y_c^*) = \frac{1}{\kappa y_c^*} \pm 2\beta. \tag{23}$$

The Coriolis region is bounded above by the requirement that the scale D does not influence the region, which imposes the following relation:

$$y/\delta_c < K_3 D/\delta_c = K_3 Re^* |\Omega| \nu/u_*^2. \tag{24}$$

The lower side of this region is bounded by different requirements depending on $K_1\delta_v > K_2\delta_c$ or $K_1\delta_v < K_2\delta_c$. In the first case, when the Coriolis force effect is not sufficient to penetrate the viscous or buffer region, the lower boundary is given as

$$y_c^* > K_2. \tag{25}$$

In the second case, $K_1\delta_v > K_2\delta_c$, when the Coriolis force is quite strong and affects the flow in the viscous or buffer region, it is given as

$$y_c^* > K_1 |\Omega| \nu/u_*^2. \tag{26}$$

Thus, the viscous effect does not appear in the Coriolis region.

Another way of expressing the velocity profile within the log and Coriolis region is to adopt the log law, equation (15), assuming that κ and C_1 are not constants but depend on Re^* and $\Omega\nu/u_*^2$ as

$$\kappa = \kappa(Re^*, \Omega\nu/u_*^2), \quad C_1 = C_1(Re^*, \Omega\nu/u_*^2). \tag{27}$$

Watmuff, Witt & Joubert (1985) and Koyama *et al.* (1979) adopted the above relation to estimate the Coriolis force effect in the log region.

2.3.3. *Core region*

The core region is an area where outer scale D is dominant while the viscous scale does not appear. Adopting D and u_* as the basic dimension set, the dimensionless expression (3) is replaced by the following relation:

$$\mathrm{d}(U/u_*)/\mathrm{d}(y/D) = f_6(y/D, \nu/u_* D, \Omega D/u_*). \tag{28}$$

When ν/Du_* and $\Omega D/u_*$ approach 0, the above equation leads to the usual defect law.

The Coriolis parameter in the core region is $\Omega D/u_*$, which means a ratio between the time scales of $1/\Omega$ and D/u_*. In the case when $\Omega D/u_*$ is quite large (i.e. an overwhelming Coriolis force), the local shear stress τ is greatly altered from non-rotating channel flow by the Coriolis force effect, so u_* is not suitable as the velocity scale there. Thus, it is appropriate to adopt u'/Ω and $u'(=(\tau/\rho)^{1/2})$ rather than D and u_* as the length and velocity scales. Then the functional form of $\mathrm{d}U/\mathrm{d}y, f_6$, that does not include D, u_* and ν, becomes

$$\mathrm{d}U/\mathrm{d}y = A\Omega. \tag{29}$$

According to the experiment of Johnston *et al.* (1972) and DNS by Kristoffersen & Anderson (1993) at high rotation rate, the constant A is estimated to be 2. Equation (29) is derived for rapidly rotating channel flow. For the moderately rotating case, no explicit expression can be obtained from dimensional considerations. The following velocity deviation is introduced from equation (29):

$$\mathrm{d}U/\mathrm{d}y - 2\Omega = u_*/Df_7(y/D, \Omega D/u_*). \tag{30}$$

Integrating this with respect to y gives the following modified defect law:

$$(U_c - U - 2\Omega\zeta)/u_* = f_7(y/D, \Omega d/u_*), \tag{31}$$

where $\zeta = D - y$ and U_c is the velocity at $y = D$.

3. Experimental apparatus and methods

Figure 4 shows the general arrangement of the rotating channel and velocity measuring system. Air from the blower first passes through an orifice plate for measuring the flow rate Q and enters the rotating system through an inlet port 1, then passes through a settling chamber 14 where a honeycomb, screens and a contraction are equipped, and finally enters the test channel. The test channel has cross-sectional dimensions of 10 × 80 mm and a total length of 2000 mm. A velocity measuring station is located at $x = 1800$ mm ($x/D = 361$) downstream from the channel inlet section, where the flow was two-dimensional and fully developed for the stationary channel. There are pressure holes at $x/D = 140$, 220 and 360 for measuring the wall static pressure. The channel can rotate around the z-axis at the prescribed angular velocity Ω. A hot-wire anemometer system is placed in the rotating frame, above of the channel, and the signals from it are transferred to the stationary frame through slip rings 7. The hot wire is made of tungsten (5 μm diameter) having a sensing length of 1 mm.

The hot-wire probe is traversed along the channel mid-plane by a gear mechanism driven by a pulse motor (0.01 mm/step). The wire closest to the wall is measured by viewing the wire and its reflection image reflected from the wall in a microscope within the accuracy of 3 μm.

Accurate velocity measurements close to the wall are crucial to estimate the friction velocity u_* from the velocity gradient to the wall. However, hot-wire anemometer measurements near the wall result in erroneous velocity data due to additional heat loss to the wall (see Bhatia, Durst & Jovanovic 1982). Various compensation formulae for this phenomenon were proposed but did not yield consistent results. We developed a new scheme to estimate u_* from the U-profile near the wall, $y^+ > 5$, where the wall effect is negligible (see Bhatia *et al.*). First, we assume that the flow has a log region (Kármán constant κ is as yet unknown). Within the log region the following relation holds:

$$y\,\mathrm{d}U/\mathrm{d}y = u_*/\kappa = \gamma = \text{constant}. \tag{32}$$

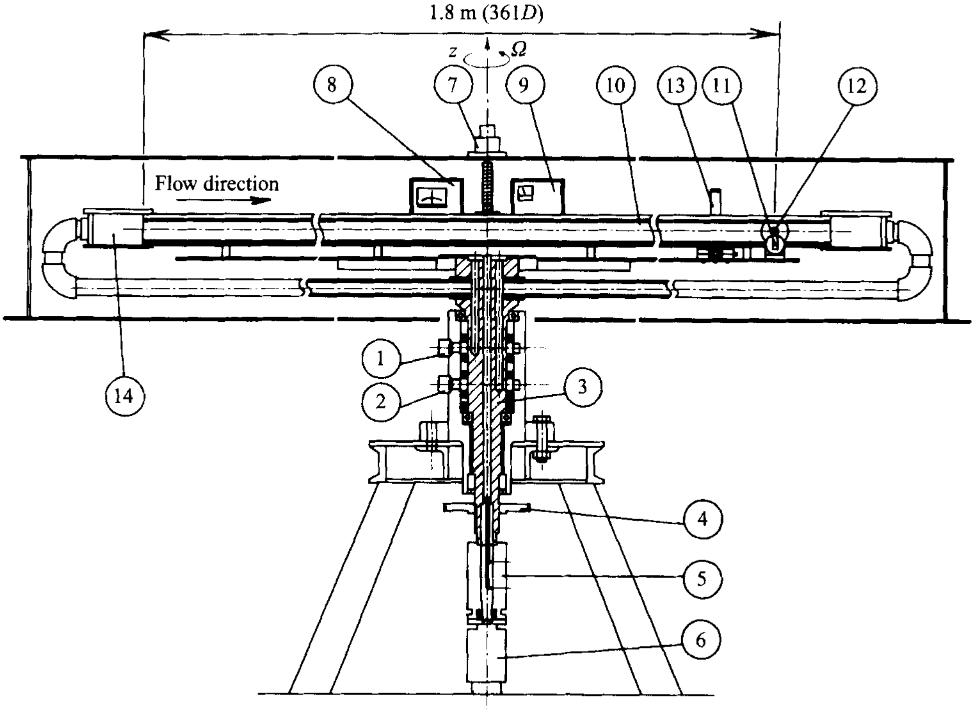

FIGURE 4. Experimental apparatus: 1, inlet port; 2, exit port; 3, rotating shaft; 4, pulley; 5, pressure taps; 6, slip ring for power supply; 7, slip ring for signal; 8, 9, hot-wire anemometer and temperature compensation units; 10, test channel; 11, traversing gear; 12, hot-wire probe; 13, microscope stand; 14, settling chamber.

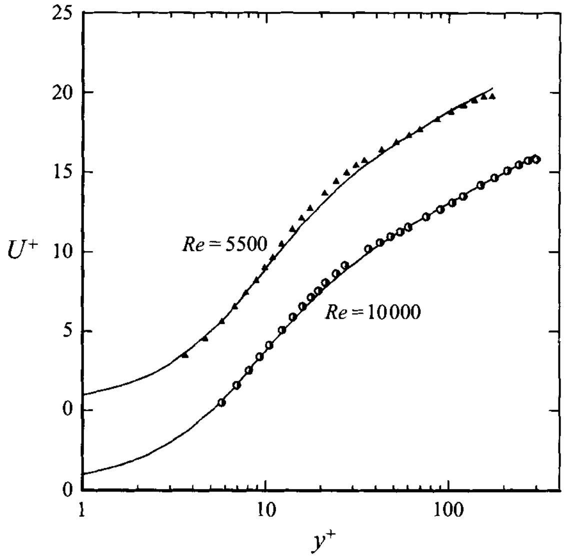

FIGURE 5. Velocity data fitting with the Van-Driest formula. —, Van-Driest velocity formula; see table 1 for symbols.

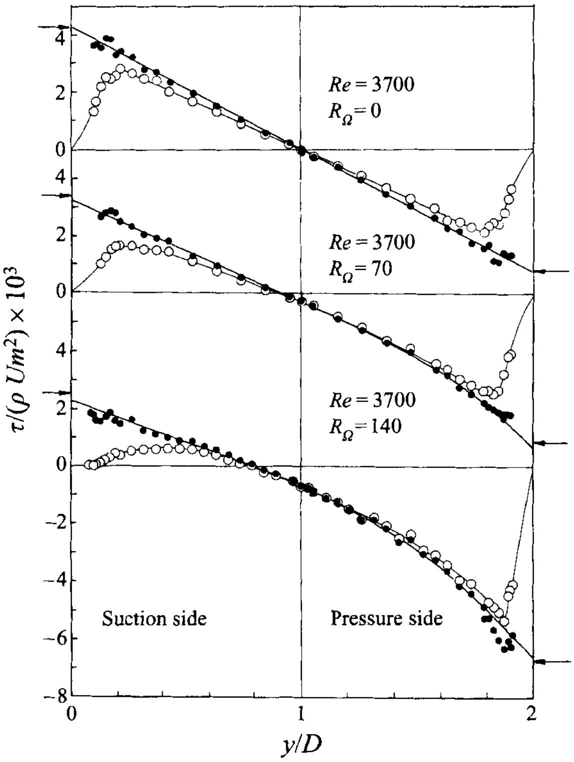

FIGURE 6. Shear stress distributions measured by ×-wires. ○, Reynolds shear stress; ●, total shear stress; Arrows indicate wall shear stress estimated by velocity fitting method.

Using the measured data in the range of the assumed log region, the constant γ in (32) can be obtained. Using u_* and γ, the Van-Driest velocity formula can be expressed as

$$U^+ = \int_0^{y^+} \frac{2\,\mathrm{d}y^+}{1+[1+4(u_* y^+/\gamma)^2\{1-\exp(-y^+/A^+)\}^2]^{1/2}}. \tag{33}$$

Here A^+ and u_* are unknowns and determined so that the functional form (33) fits best the measured velocity profile in the range of $5 < y^+ < 100$. Then the Kármán constant κ can be calculated from (32). Figure 5 shows examples of the fitting for a stationary channel at $Re = 5500$ and 10000. When the logarithmic velocity profile does not exist, in low Reynolds number flow, the velocity gradient method should be used instead of the above method. To evaluate the velocity gradient at the wall, the wall corrections are applied to the measured velocity by subtracting the additional velocity caused by the wall effect. Figure 6 compares the wall shear stresses estimated by the above methods (indicated by arrows) with those obtained by extrapolating to the wall the measured total shear stress using a ×-wire. The differences in τ_w between the two methods are typically within $\pm 5\,\%$.

For the stationary channel, $R_\Omega = 0$, the measured shear stress follows the linear distribution of fully developed flow. Considering the long inlet length adopted here ($x/D = 361$), the rotating channel flows are also considered to be fully developed. Further, the static pressures measured at three streamwise sections with and without rotation follow linear profiles from which the friction factor can be calculated. This is another confirmation of the fully developed flow.

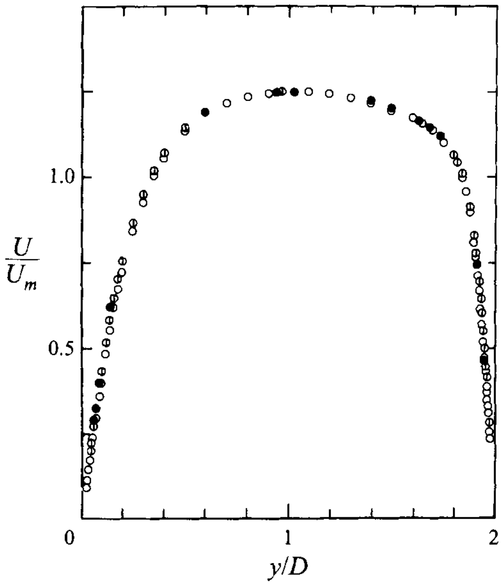

FIGURE 7. Velocity distributions measured at three spanwise sections for $Re = 3700$, $R_\Omega = 140$. Sections: ●, $Z = 0$ mm; ⦶, $Z = 5$ mm; ○, $Z = 10$ mm.

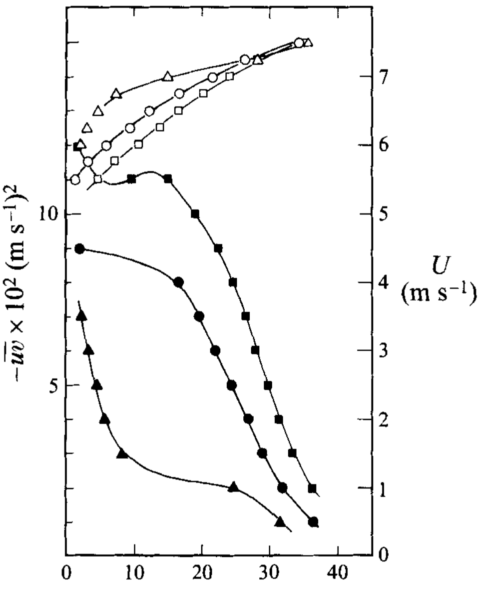

FIGURE 8. Spanwise variation of velocity and shear stress distributions reproduced from figure 14 of Watmuff *et al.* (1985). Velocity: ○, $Z = 0$ mm; △, $Z = 40$ mm; □, $Z = -10$ mm. Reynolds shear stress: ●, $Z = 0$ mm; ▲, $Z = 40$ mm; ■, $Z = -10$ mm.

The shear stress profiles for the rotating channel at $Re = 3700$ and $R_\Omega = 70$ and 140 in figure 6 are curved on the pressure side in contrast to the straight ones expected for the fully developed two-dimensional flow. The main reason for the curved profile is the existence of roll cells developed on the pressure side because V and W (where V and

Run	$Re = \dfrac{2DU_m}{\nu}$	$R_\Omega = \dfrac{4D^2\lvert\Omega\rvert}{\nu}$	$R_0 = \dfrac{2D\lvert\Omega\rvert}{U_m}$	$Re^* = \dfrac{Du_*}{\nu}$	$\dfrac{\Omega\nu}{u_*^2}$	$\dfrac{\Omega D}{u_*}$	Symbol
1	1700	0	0.0000	67	0.00000	0.0000	○
2		27P	0.0159	78	0.00110	0.0864	·
3		74P	0.0435	79	0.00290	0.2350	⊞
4		27S	0.0159	58	−0.00197	−0.1150	·
5		47S	0.0276	56	−0.00369	−0.2080	
6		74S	0.0435	58	−0.00573	−0.3250	⊞
7	2500	0	0.0000	99	0.00000	0.0000	⊕
8		27P	0.0108	103	0.00064	0.0658	
9		74P	0.0296	110	0.00153	0.1680	⊗
10		145P	0.0547	118	0.00262	0.2900	⬗
11		27S	0.0108	90	−0.00083	−0.0750	
12		74S	0.0296	74	−0.00334	−0.2480	⊗
13		145S	0.0547	77	−0.00575	−0.4430	⬗
14	3700	0	0.0000	122	0.00000	0.0000	□
15		70P	0.0189	133	0.00099	0.1330	⦶
16		120P	0.0324	137	0.00160	0.2330	⊖
17		140P	0.0378	157	0.00142	0.2230	
18		70S	0.0189	106	−0.00156	−0.1630	⧄
19		120S	0.0324	94	−0.00343	−0.3160	◇
20		140S	0.0378	95	−0.00387	−0.3680	
21	4500	0	0.0000	145	0.00000	0.0000	●
22		70P	0.0156	154	0.00073	0.1140	◪
23		120P	0.0267	157	0.00122	0.1910	⟐
24		70S	0.0156	134	−0.00095	−0.1300	◈
25		120S	0.0267	123	−0.00197	−0.2440	◆
26	5500	0	0.0000	174	0.00000	0.0000	▲
27		70P	0.0127	182	0.00053	0.0959	⊙
28		120P	0.0218	183	0.00089	0.1630	⬙
29		70S	0.0127	168	−0.00062	−0.1040	⍋
30		120S	0.0218	159	−0.00119	−0.1890	⍒
31	8000	0	0.0000	234	0.00000	0.0000	■
32		120P	0.0150	252	0.00047	0.1190	⟠
33		120S	0.0150	231	−0.00056	0.1300	◫
34	10000	0	0.0000	300	0.00000	0.0000	◑
35		120P	0.0120	310	0.00031	0.0970	▽
36		120S	0.0120	291	−0.00035	−0.1030	▼

TABLE 1. Experimental conditions. For definitions see the text

W are wall-normal and spanwise velocity components) can affect the shear stress profile as

$$\tau = \tau_w + \frac{\mathrm{d}p}{\mathrm{d}x}y + \rho\int_0^y\left(V\frac{\partial U}{\partial y} + W\frac{\partial U}{\partial z} - 2\Omega v\right)\mathrm{d}y. \tag{34}$$

From this indirect evidence, it is conjectured that roll cells exist on the pressure side. Because of these roll cells, the flow in the rotating channel is not considered to be two-dimensional on the pressure side even in the mid-plane. Figure 7 shows the velocity profiles ($Re = 3700$, $R_\Omega = 140$) measured at three different spanwise section $z = 0$ (mid-plane), 5 and 10 mm. No appreciable difference can be seen among them despite the roll cells. This difference in sensitivity of shear stress and velocity profiles to the roll cells is also seen in Watmuff *et al.* (1985). They measured the spanwise variations of mean velocity and Reynolds stresses in developing turbulent boundary layers with system rotation. Figure 8, reproduced from figure 14 in their paper, shows that the variation of the shear stress profile is far greater than that of mean velocity. Also, comparison between figures 6 and 17(*a*) in their paper confirms that the spanwise variation of the wall-law profile is greatly exceeded by the variation caused by the Coriolis stabilizing/destabilizing effect itself. Thus, even though the roll cells are unavoidable in the rotating channel, the mean velocity profiles measured in the mid-plane are not substantially altered by them.

The experimental uncertainties in mean velocity U and wall shear stress τ_w are estimated to be $\pm 2\%$ and $\pm 5\%$ of their values (20:1 odd), respectively.

The experiments are performed under the conditions shown in table 1. The mean axial velocity U_m appearing in *Re* and *Ro* is defined as Q/(cross-sectional area of the channel). Positive values of $\Omega\nu/u_*^2$ and $\Omega D/u_*$ are for the pressure side, while negative ones are for the suction side. The letters P and S after the rotational Reynolds number $R_\Omega = (2D)^2|\Omega|/\nu$ indicates the pressure and suction side of the channel, respectively. Symbols given in the table for each run are used in the figures unless otherwise indicated in the caption.

4. Experimental results and discussion

4.1. *Friction factor and skin friction coefficient*

Figure 9 shows the variation of friction factor λ with *Re* for various R_Ω. The friction factor is defined by

$$\lambda = \Delta p \frac{2D}{\Delta x}/(\rho U_m^2/2), \tag{35}$$

where Δp is the pressure drop between $x/D = 220$ and 360. The stationary channel data coincide quite well with the theoretical curve for a channel of aspect ratio eight in the laminar region and with a Blasius formula in the turbulent region. As R_Ω is increased, λ increases in the laminar region due to the development of the roll cells (see Speziale & Thangam 1983). In the turbulent region, λ does not change much with R_Ω. This constancy of λ is because the increase of τ_w on the pressure side is just cancelled out by the decrease of τ_w on the suction side.

Figure 10 shows the relation between the skin friction coefficient C_f, defined as $C_f = 2\tau_w/(\rho U_m^2)$, and *Re* for stationary and rotating channel flows. From the stationary channel data the transition to turbulent flow occurs between $Re = 1500$ and 1700. In the turbulent region C_f almost coincides with the empirical formulae proposed by Dean (1978) or Johnston *et al.* (1972). For the rotating channel flow, the value of C_f increases at the pressure side and decreases at the suction side in relation to the stationary channel value with increasing R_Ω. The rate of change becomes larger as the Reynolds number is reduced if the rotation Reynolds number R_Ω is the same. This means that there is a strong Reynolds number dependence of the Coriolis force effect on the turbulent flow. This *Re*-dependence can be seen in the flow regime diagram. In the parameter plane of figure 3, $R_\Omega =$ const. can be expressed as

$$2\ln Re^* + \ln(|\Omega|\,\nu/u_*^2) = \text{const.} \tag{36}$$

The line P–Q on the *aOb* plane in figure 3 is the $R_\Omega =$ constant line. The line projected on the K_2-plane, P–Q′, shows that as Re^* decreases, the Coriolis force penetrates inside,

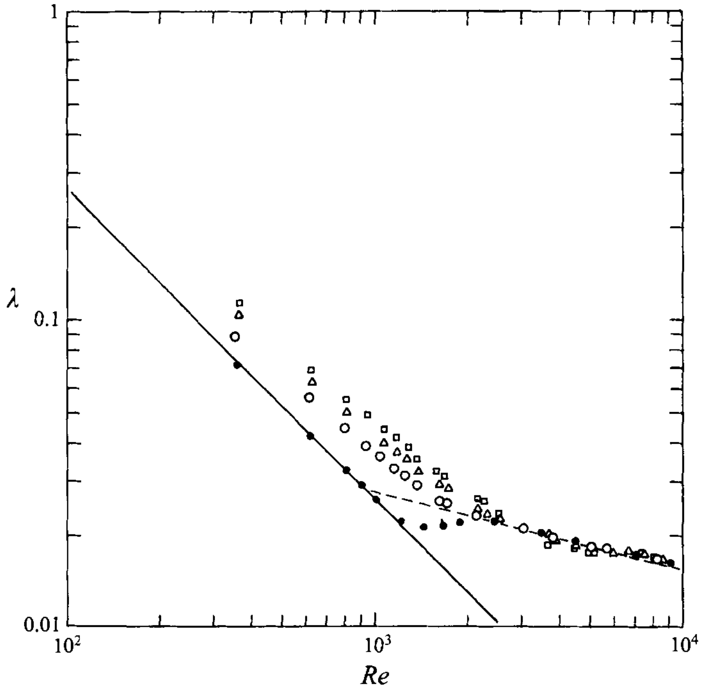

FIGURE 9. Friction factor: —, $\lambda = 26.1/Re$ (theoretical line for aspect ratio 8 in laminar flow); ----, $\lambda = 0.154\ Re^{-1/4}$ (Blasius formula); ●, $R_\Omega = 0$; ○, 27; △, 74; □, 145.

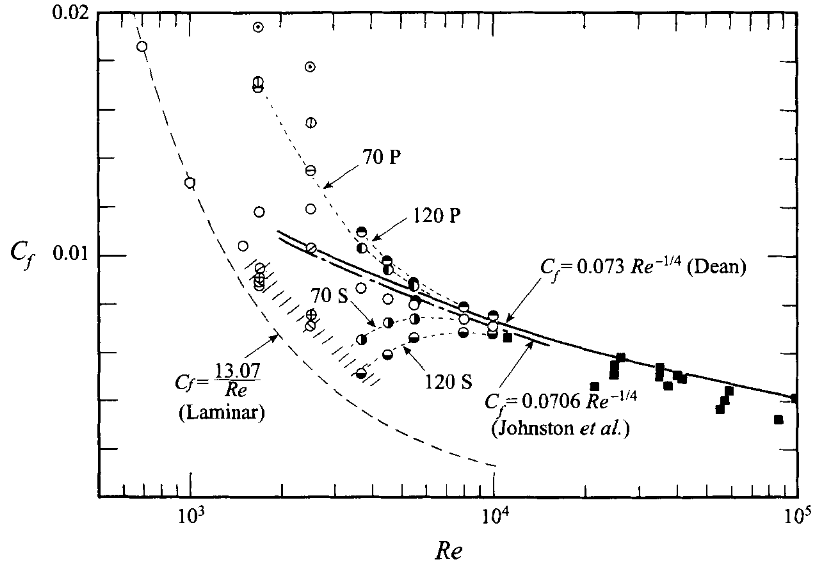

FIGURE 10. Skin friction coefficient Non-rotating channel flow; ----laminar flow for aspect ratio of 8; —, empirical formula by Dean (1978); ----, empirical formula by Johnston *et al.* (1972); ●, DNS by Kim *et al.* (1987); ■, other data reproduced from Dean. Present data for rotating channel flow: ○, $R_\Omega = 0$; ⊖, 27P; ⊘, 27S; ◐, 70P; ◑, 70S; ⦶, 74P; ⊕, 74S; ◓, 120P; ◒, 120S; ⊙, 145P; ⊗, 145S; /////////, relaminarized region.

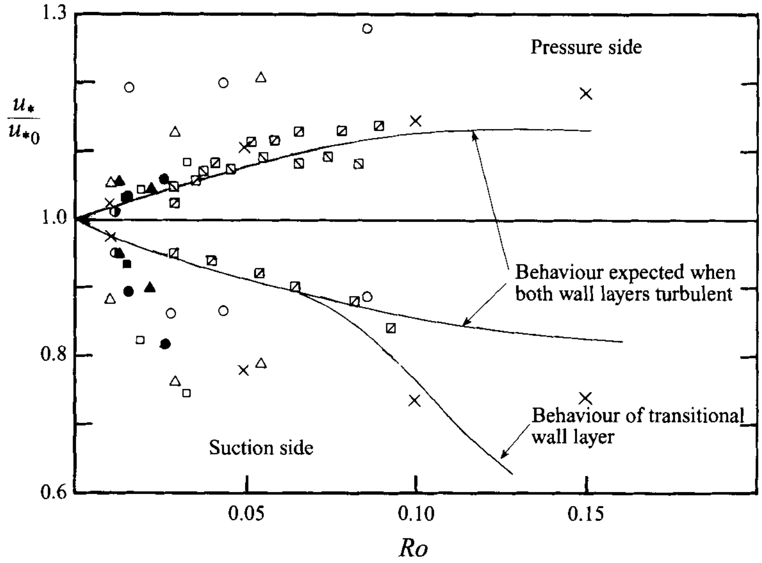

FIGURE 11. Friction velocity ratio versus rotation number. Johnston *et al.* (1972): —, $Re = 10000$; ▨, 25700; ▧, 33100. Kristoffersen & Andersson (DNS, $Re = 5800$): ×. Present: ○, $Re = 1700$; △, 2500; □, 3700; ●, 4500; ▲, 5500; ■, 8000; ◑, 10000.

i.e. smaller y^+, thus a strong Coriolis effects appears in the wall region. Physically, this result can be understood as when Re decreases, rotation acts on weaker turbulence so that it can modify the turbulence more easily.

At the suction side, C_f decreases as R_Ω increases and finally approaches the values (hatched region in figure 10) far below the stationary channel value but slightly higher than the laminar flow value (broken line). Here the flow is considered to be relaminarized by the Coriolis stabilizing effect. Since the difference in C_f between non-rotating and relaminarized flows increases as Re increases, the rate of reduction of C_f in the relaminarized flow increases with Re.

In the literature to date, the Coriolis force effect on the wall shear stress was indicated by variations of the friction velocity ratio u_*/u_{*0} (where u_{*0} represents the friction velocity without rotation) against the rotation number $Ro = 2|\Omega|D/U_m$ as shown in figure 11. There, the data for various Reynolds numbers are compared. The present data as well as the DNS data of Kristoffersen & Andersson (1993), all for $Re < 10000$, do not coincide with those of Johnston *et al.* (1972) measured at high Reynolds number. There is an appreciable Reynolds number dependence among the data.

As described in §2, $\Omega\nu/u_*^2$ is a relevant parameter describing the Coriolis force effect close to the wall. It is expected that the Re-dependence of u_*/u_{*0} in figure 11 would be absorbed into a parameter $\Omega\nu/u_*^2$. The present data and those of Johnston *et al.* (1972) and Kristoffersen & Andersson (1993) are plotted in figure 12 using this new parameter.

The data on the suction side are well correlated with the empirical relation

$$(u_*/u_{*0})^2 = C_f/C_{f_0} = 1.0 + 160\Omega\nu/u_*^2 \tag{37}$$

(indicated by a solid line in the figure) in the range $\Omega\nu/u_*^2 > -2.3\times10^{-3}$ and $Re > 2500$. The data for $Re \geqslant 2500$ deviate from (37) in the range $\Omega\nu/u_*^2 \leqslant -2.3\times10^{-3}$, whereas

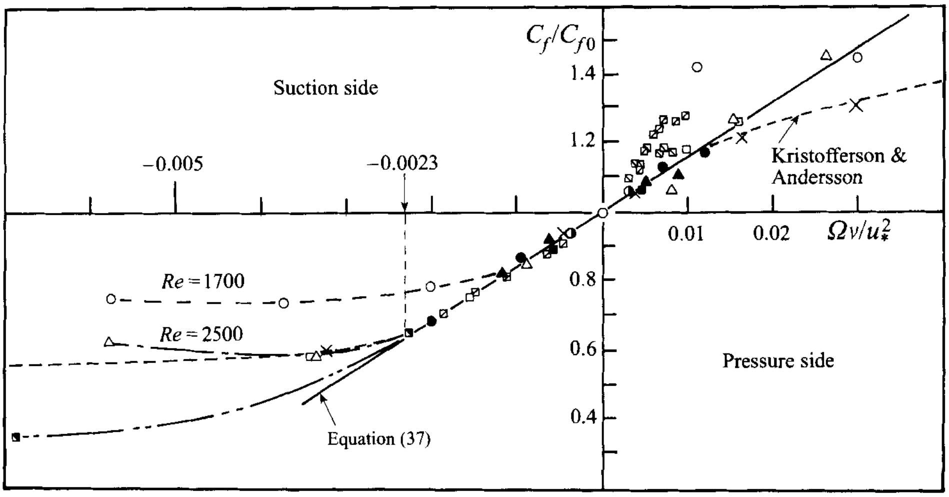

FIGURE 12. Skin friction coefficient ratio against $\Omega\nu/u_*^2$. For symbols see figure 11. Additional data from Johnston *et al.* (1972): ◪, $Re = 11400$.

the data for $Re < 2500$ deviate somewhere between -2.3×10^{-3} and 0, depending on the Reynolds number of the flow. The off-line data are considered to be relaminarized flow from various evidence, such as the C_f value in figure 10, the velocity distribution plotted on the semi-log graph shown later in figure 18 or the flow visualization of Johnston *et al.* (1972). A further decrease in the parameter from the point of deviation makes C_f slightly lower and finally almost constant. The rate of reduction of C_f from its stationary channel flow value increases with Re.

It is conjectured that the relaminarization on the suction side occurs in two different ways, depending on whether or not the Reynolds number exceeds about 2500. In the case of $Re \geqslant 2500$, relaminarization occurs when $\Omega\nu/u_*^2 = -2.3 \times 10^{-3}$; in this case the Coriolis stabilizing effect is a main reason for the flow reversion to laminar. When $Re < 2500$, the criterion for the relaminarization depends not only on the Coriolis parameter but also on the Reynolds number. The Coriolis force reduces u_* and stabilizes the turbulent motion on the suction side. When the Reynolds number is low, say less than 2500, u_* is reduced by the Coriolis force to below the level necessary to sustain the turbulent activity before the Coriolis direct stabilizing effect relaminarizes it. The lower the Re of the flow, the smaller the $\Omega\nu/u_*^2$ necessary to reduce u_* below the critical level, and the relaminarization depends on both Re and $\Omega\nu/u_*^2$.

On the pressure side, some dispersion is seen among the data and the empirical relation of equation (37) indicates merely their average trend. One possible reason for this is that the wall shear stress on the pressure side may have some inhomogeneity in the spanwise direction due to the roll cells appearing on the pressure side as indicated by Watmuff *et al.* (1985), who reported more than a 15% variation in C_f in the spanwise direction.

4.2. *Velocity profiles at low Reynolds number in a stationary channel*

Before showing velocity profiles in a rotating channel, it is useful to show various aspects of the low Reynolds number flow in a stationary channel. The overall accuracy of the experimental data presented in this paper can also be estimated by comparing the measured data with others obtained for a stationary channel.

Figure 13 shows the semi-log plot of measured mean velocity profiles in the low

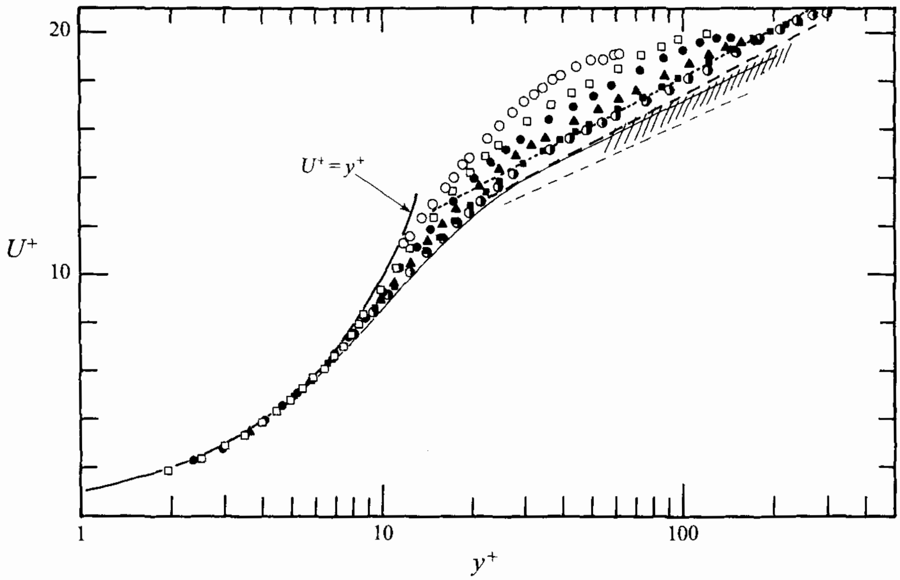

FIGURE 13. Mean velocity profile for non-rotating channel. See table 1 for symbols. ------, Comte-Bellot ($Re = 57000$); ---, Clark ($Re = 14400$); —, Kim *et al.* (DNS, $Re = 5600$); ---, Hussain & Reynolds ($Re = 13800$); ///////, Antonia *et al.* ($Re = 2DU_c/\nu = 6600$–43000; U_c is centreline velocity).

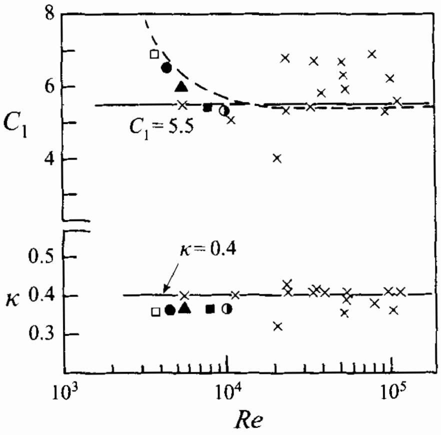

FIGURE 14. Constants κ and C_1 in a log-law plot against Re. See table 1 for symbols. ×, Reproduced from Dean; ---, Patel & Head.

Reynolds number range ($1700 \leqslant Re \leqslant 10000$). The velocity profiles shift downward as Re increases and finally settle on the high Reynolds number universal wall-law profile when $Re \geqslant 8000$. Comparisons of the profiles of $Re = 8000$ and 10000 with others of high Reynolds number reveal that the present data are consistent with those of Comte-Bellot (1963) and Clark (1968), but about 10% higher than those of Hussain & Reynolds (1975). The recent experimental data of Antonia *et al.* (1992) for a universal log law are shown by the hatched band located between the present and Hussain & Reynolds profiles. From these comparisons, it is conjectured that the measured U^+ is about 5% larger than the typical U^+ obtained by previous workers.

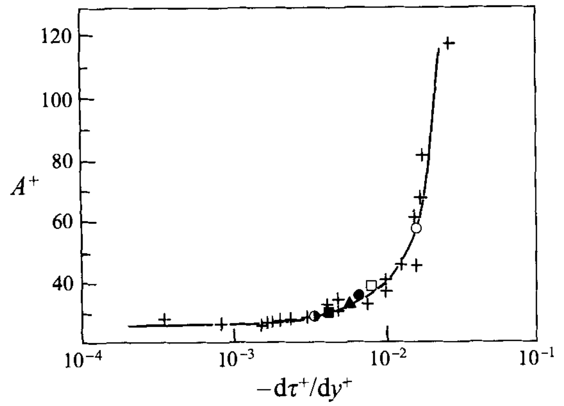

FIGURE 15. Van-Driest damping factor A^+ versus shear stress gradient. See table 1 for symbols. +, Huffman & Bradshaw.

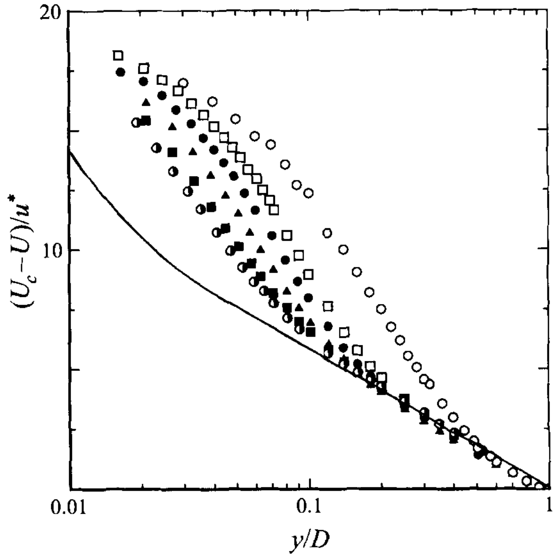

FIGURE 16. Velocity defect-law for non-rotating channel flow. See table 1 for symbols. —, Hussain & Reynolds.

The Re-dependence of the velocity profile can be expressed as variations of constants C_1 and κ with Re (see (27)), figure 14. The data below $Re = 4500$ in this figure should be taken with some reservation, for some subjective line-fitting was done in the log region. It shows that C_1 increases from around 5 at $Re = 10000$ as Re decreases. The present result is in good agreement with that obtained by Patel & Head (1969) for pipe flows (see the broken line in the figure). However, κ does not change with Re. As the Reynolds number decreases, the effect of the outer scale D on the turbulence appears in the buffer region and changes the structure of turbulence there, causing C_1 to change with Re. Huffman & Bradshaw (1972) adopted the Van-Driest damping factor A^+ to express the change of velocity profile in the buffer region in low Reynolds number flows. Figure 15 shows how A^+ changes with Re^*. (In the figure shear stress gradient $-d\tau^+/dy^+$ is used as the abscissa instead of Re^* in accordance with Huffman &

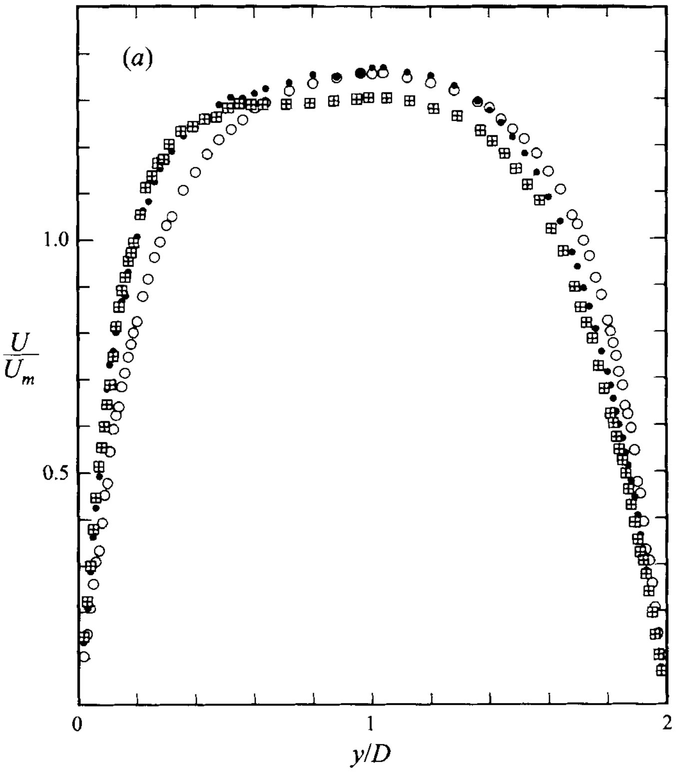

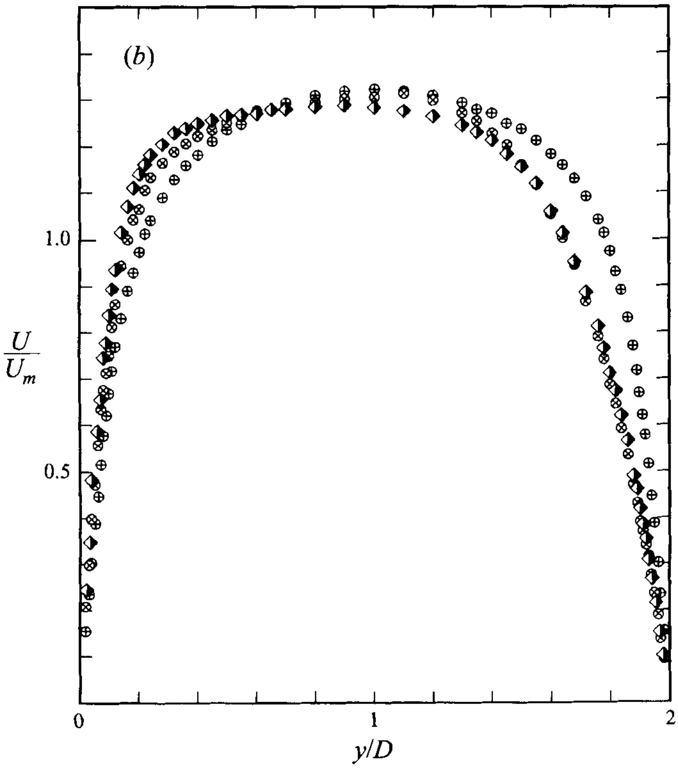

FIGURE 17 (*a*, *b*). For caption see next page.

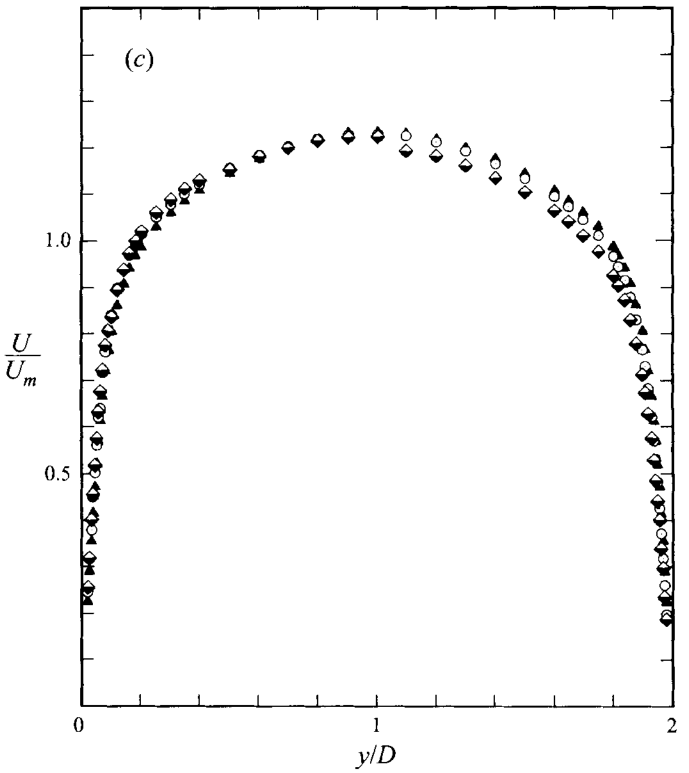

FIGURE 17. Velocity profiles U/U_m against y/D. (a) $Re = 1700$: ○, $R_\Omega = 0$; ●, $R_\Omega = 27$; ⊞, $R_\Omega = 74$. (b) $Re = 2500$: ⊕, $R_\Omega = 0$; ⊗, $R_\Omega = 74$; ⬗, $R_\Omega = 145$. (c) Re $= 5500$: ▲, $R_\Omega = 0$; ⊙, $R_\Omega = 70$; ⬙, $R_\Omega = 120$.

Bradshaw.) In fully developed channel flow, $-\mathrm{d}\tau^*/\mathrm{d}y^+ = Re^{*-1}$. At high Reynolds number, $A^+ = 26$, and it increases as Re^* decreases. The present results agree quite well with Huffman & Bradshaw's result.

Figure 16 indicates the velocity defect law for various Reynolds numbers. The present data deviate upward from the high Reynolds number profile of Hussain & Reynolds (1975), at some y/D. The y/D position where the data start to deviate from the high-Re line depends on the Reynolds number of the flow; the lower the Re, the larger the value of y/D. This means that the viscous effect penetrates the central part of the channel as Re (or Re^*) decreases. If the position y/D is expressed by wall variables, it is always around 30–50 irrespective of Re. This indicates that the constant K_1 in (6a) is about 30–50.

4.3. *Velocity profiles at low Reynolds number in a rotating channel*

Figure 17 shows the velocity profiles U/U_m versus y/D in a rotating channel at quite lower Reynolds numbers ($Re = 1700$, 2500 and 5500). The overall velocity profile measured at Re higher than 5500 and at $R_\Omega = 120$ is very similar to that for the stationary channel. Since the velocity profiles are measured only along the half-channel width, $0 \leqslant y \leqslant D$, with positive or negative Ω, the suction-side profiles are displaced to the other side of the channel, $D \leqslant y \leqslant 2D$, and connected with the pressure-side profile to make the full profile shown in the figure. Thus a small discontinuity at the junction point ($y = D$) is unavoidable. The qualitative features of the overall change of the

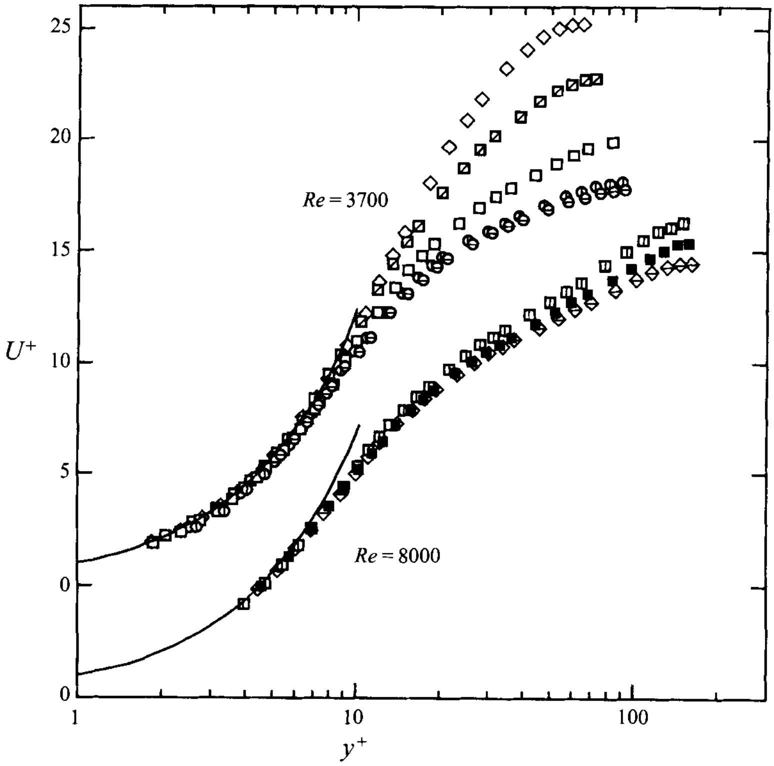

FIGURE 18. Velocity profile for rotating channel flow. See table 1 for symbols. Solid lines show $U^+ = y^+$.

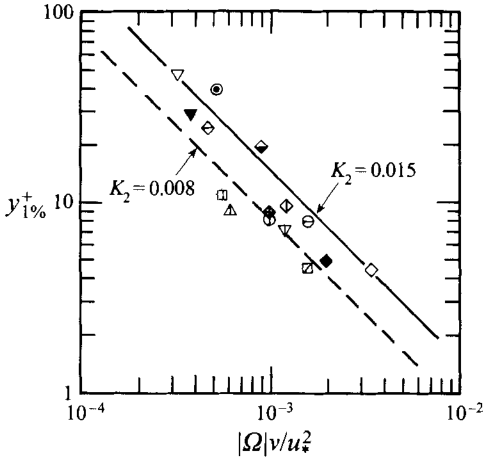

FIGURE 19. Coriolis force penetrating distance. See table 1 for symbols.

profile due to the Coriolis force are the same as reported by Johnston *et al.* (1972) and Kristoffersen & Andersson (1993).

Mean velocity profiles in a rotating channel presented using wall variables are shown in figure 18 for $Re = 3700$ and 8000. As generally acknowledged, owing to the Coriolis force effect the suction-side profiles shift upward from the non-rotating conventional

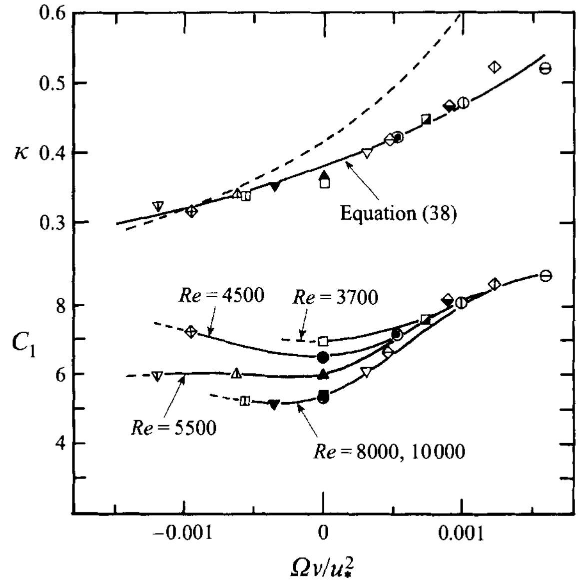

FIGURE 20. Constants κ and C_1 against $\Omega\nu/u_*^2$. See table 1 for symbols. ----, Watmuff *et al.*

wall law, whereas the profiles for the pressure side shift downward. The deviations from the conventional log law increase with R_Ω and largely depend on the Reynolds number of the flow. From this figure it can be seen that the Coriolis force effect penetrates the wall region as R_Ω increases or Re decreases. The depth of penetration, if expressed using a wall variable, depends only on $|\Omega|\nu/u_*^2$ as shown in §2. Here we introduce $y_{1\%}^+$, that is the distance from the wall at which the velocity profile deviates by 1% from the non-rotating profile. To estimate $y_{1\%}^+$ the velocity profiles are compared in their interpolated forms using the Akima (1972) interpolation method. This $y_{1\%}^+$ is a measure of the distance the effect of the Coriolis force penetrates. Figure 19 shows the relation between $y_{1\%}^+$ and $|\Omega|\nu/u_*^2$. Although there is some scatter among the data, $y_{1\%}^+$ decreases monotonically along a line irrespective of the Reynolds number. The lines in the figure show equation (6*b*) with particular K_2 values. From this figure the constant K_2 is found to be 0.008–0.015.

The mean velocity profile variation in a rotating channel like the one presented in figure 18 can be seen as variations of the constants κ and C_1. They depend on Re^* (or Re) and $\Omega\nu/u_*^2$, see equation (27), as shown in figure 20. Similar to the stationary channel flow, the Kármán constant κ is independent of the Reynolds number but varies with $\Omega\nu/u_*^2$ in a rotating channel. An empirical formula for κ is

$$1/\kappa = 2.63 - 4.94\Omega\nu/u_*^2. \tag{38}$$

This relation differs from that of Watmuff *et al.* (1985), developed for boundary layer flow, shown by the broken line in the figure. It is not clear why there is a difference between the channel and boundary layer flows. The constant C_1 depends on both Re and $\Omega\nu/u_*^2$. For the non-rotating flow shown in figure 14, C_1 is substantially constant when $Re \geqslant 8000$ ($Re^* \geqslant 230$). In a rotating channel a similar consequence holds: when $Re \geqslant 8000$, C_1 depends only on $\Omega\nu/u_*^2$; however, it depends on both of them when $Re < 8000$. Even in the case of Re smaller than 8000, the friction velocity u_* increases with $\Omega\nu/u_*^2$ on the pressure side and Re^* becomes large (i.e. the flow is analogous to high

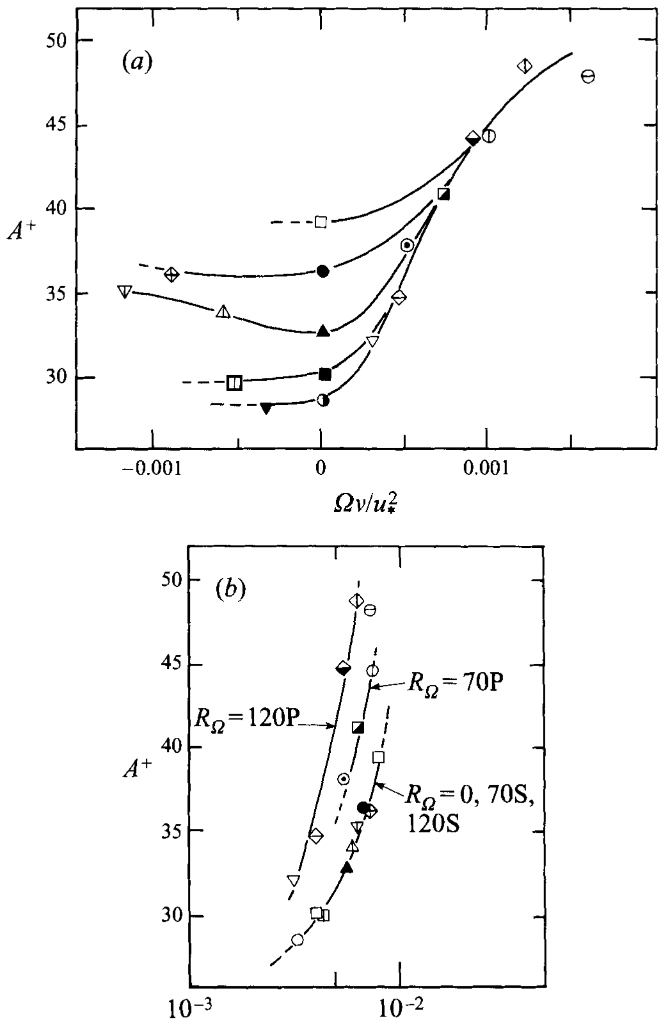

FIGURE 21. Variation of A^+ against (*a*) $\Omega\nu/u_*^2$ and (*b*) $-\mathrm{d}\tau^+/\mathrm{d}y^+$. See table 1 for symbols.

Reynolds number flow). This is why the family of C_1 curves for different Re converge into a single curve where $\Omega\nu/u_*^2 > 1.0\times10^{-3}$. The variations of constants C_1 with Re and $\Omega\nu/u_*^2$ can be expressed as variations of A^+ if the Van-Driest velocity model is adopted. Figure 21 (*a*) shows that A^+ does not change much from the non-rotating flow on the suction side, whereas it increases significantly with $\Omega\nu/u_*^2$ on the pressure side. Since A^+ reflects the structure of turbulence in the buffer region, some structural change, such as the contribution of sweeps or ejections to the Reynolds stress (see Miyake & Kajishima 1986), is expected on the pressure side. Figure 21 (*b*), where A^+ is plotted against $-\mathrm{d}\tau^+/\mathrm{d}y^+$, shows this tendency more clearly. Both the non-rotating and suction-side data follow a single curve, consistent with the results of Huffman & Bradshaw (1972), whereas the pressure-side data follow different curves depending on R_Ω.

Another way of describing the velocity profile change is as a deviation from the conventional log law ΔU^+ against y^+. As given by (19), ΔU^+ changes linearly with y^+.

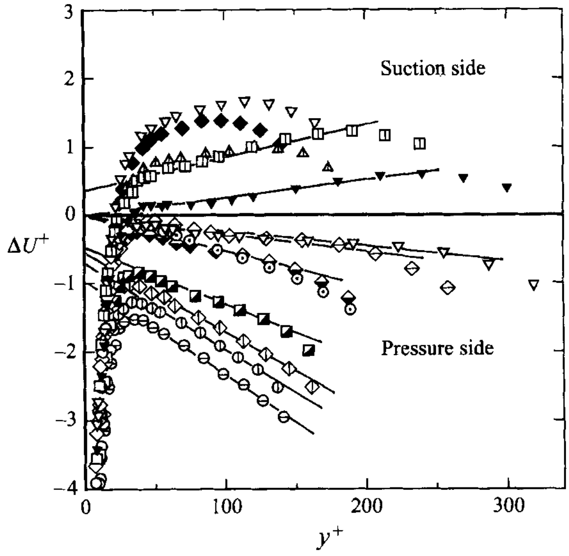

FIGURE 22. Velocity deviation from conventional log–law ΔU^+. See table 1 for symbols.

$\Omega\nu/u_*^2$	-0.00056	-0.00035	0.00031	0.00047	0.00089	0.00122
β	4.2	3.6	3.5	2.8	2.8	4.5

TABLE 2. The Monin–Oboukov coefficient, β

Figure 22 confirms that the relation holds true in the range $y^+ > 50$, except when the flow is relaminarized. There are two types of lines, one passing through the origin and the other not doing so. Lines passing through the origin indicate the flows for which the additive constant $C_2 = C_1$ because the Coriolis force effect is not strong enough to change the buffer region flow. The latter lines correspond to the flows whose constant C_2 is changed from C_1 by the effect of the Coriolis force. From the slope of these lines, the Monin–Obukhov coefficient β can be obtained using (19). Table 2 shows β obtained for various $\Omega\nu/u_*^2$. The values are distributed around 3–4. Among the many proposals relating to the coefficient β, So (1975) indicated that $\beta = 4$–6 is the most promising estimation to fit various experimental results. The present result also confirms this suggestion.

As the rotation rate increases, the log region is penetrated by the Coriolis force effect, and the Coriolis region appears as described in §2. Figure 23(a, b), where the relations between $\mathrm{d}U^+/\mathrm{d}y_c^*$ and y_c^* for various conditions are shown, confirms the existence of this region. The solid line indicates equation (23) derived for the Coriolis region, assuming the constants $\kappa = 0.4$ and $\beta = 4$. The data points for each flow condition partly follow the line as is expected from the theory developed in §2. Figure 24(a, b) shows the ranges of the Coriolis region, estimated from figure 23, by vertical lines with symbols at the top and bottom. From the theoretical consideration in §2, the Coriolis region is bounded by three relations, (24)–(26). In figure 24 the possible y_c^* range of the Coriolis region satisfied by these three relations is shown versus $Re^* |\Omega| \nu/u_*^2$, where the constants K_1, K_2 and K_3 are assumed to be 50, 0.015 and 0.3, respectively. The relations (24) and (25) are drawn by solid lines, while (26) is drawn by broken lines for various

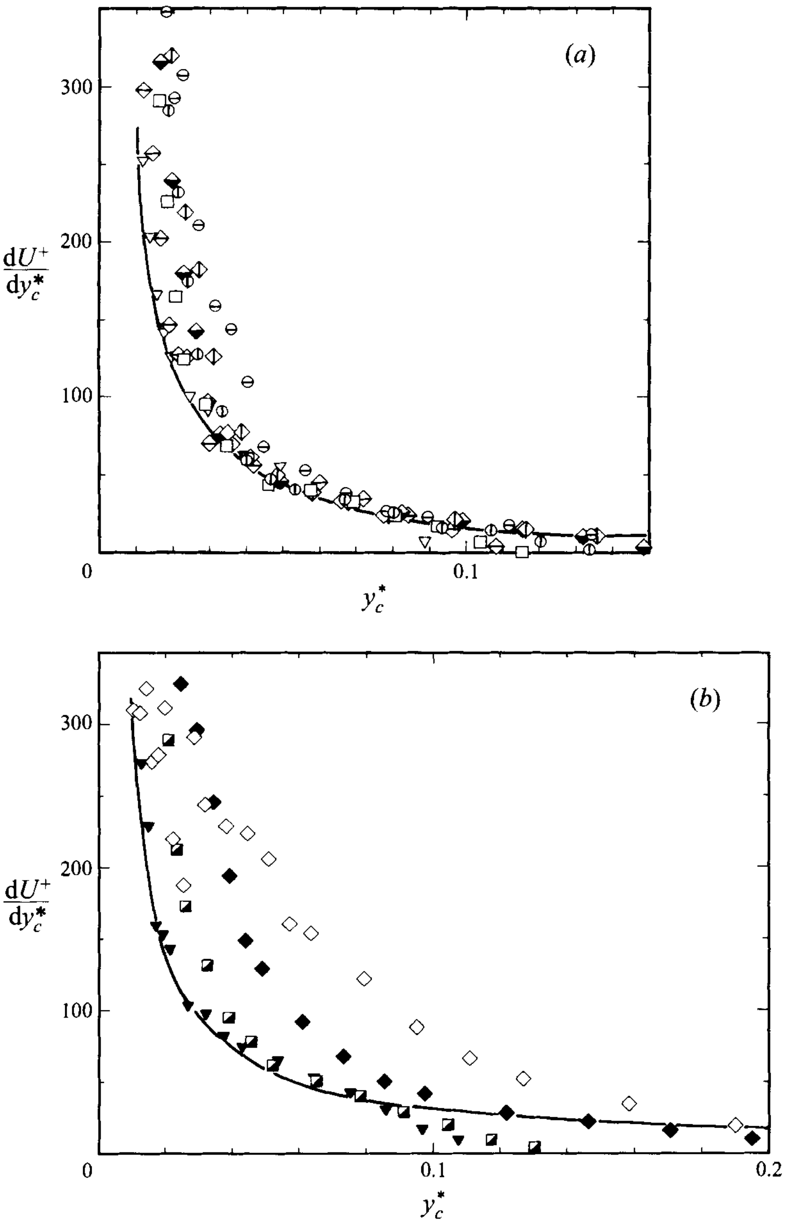

FIGURE 23. Relation dU^+/dy_c^* versus y_c^*: (a) pressure side, (b) suction side. See table 1 for symbols.

values of Re^*. Since the slope of a broken line, K_1/Re^*, becomes steeper as Re^* decreases, it coincides with the line of equation (24) when $Re^* = K_1/K_3$ (= 170). This means that the Coriolis region, shown hatched, does not exist when $Re^* < 170$. However, the experimental results show that in fact it does exist even for lower Re^* conditions. This is because there is a marginal region where (24) is not satisfied yet the velocity follows the Coriolis region formula. To include this marginal region in the Coriolis region, the constant K_3 should be altered from 0.3 to 0.7. The lower boundary of the Coriolis region, given by (26), is in good agreement with the experimental results.

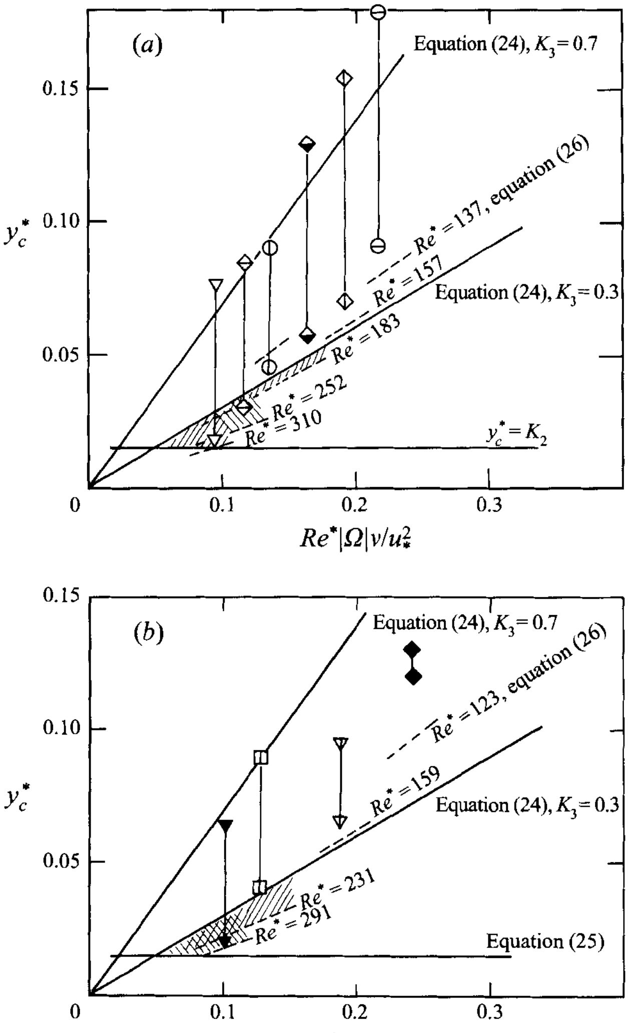

FIGURE 24. The range of the Coriolis region: (*a*) pressure side, (*b*) suction side. See table 1 for symbols. Hatched regions are predicted from equations (24) to (26) by assuming K_1, K_2 and K_3 to be 50, 0.015 and 0.3.

Core region velocity profiles expressed by the modified defect law using the relation (31) are shown in figure 25(*a*, *b*). For simplicity, we indicate only the data for $Re = 10000$ and 3700. As for high-$|\Omega| D/u_*$ flows, the data of Johnston *et al.* (1972) and Kristoffersen & Andersson (1993) are reproduced. On the pressure side, in figure 25(*a*), it is seen that the velocity follows the defect law, equation (31), where the velocity distribution depends only on $\Omega D/u_*$. The range of the defect law depends on *Re*, for example $0.1 < 1.0 - \zeta/D$ for $Re = 10000$ (open-headed arrow) and $0.2 < 1.0 - \zeta/D$ for $Re = 3700$ (solid-headed arrow). The velocity lies below the profile for the non-rotating flow and approaches zero as $\Omega D/u_*$ increases. When $\Omega D/u_* > 1.6$, it lies on the base line (zero value), and the distribution does not change thereafter. This means that most of the core region has zero mean absolute vorticity when $\Omega D/u_* > 1.6$.

On the suction side, however, there is no obvious pattern for the velocity distributions (figure 25*b*). As a whole, the velocities are distributed above the profile

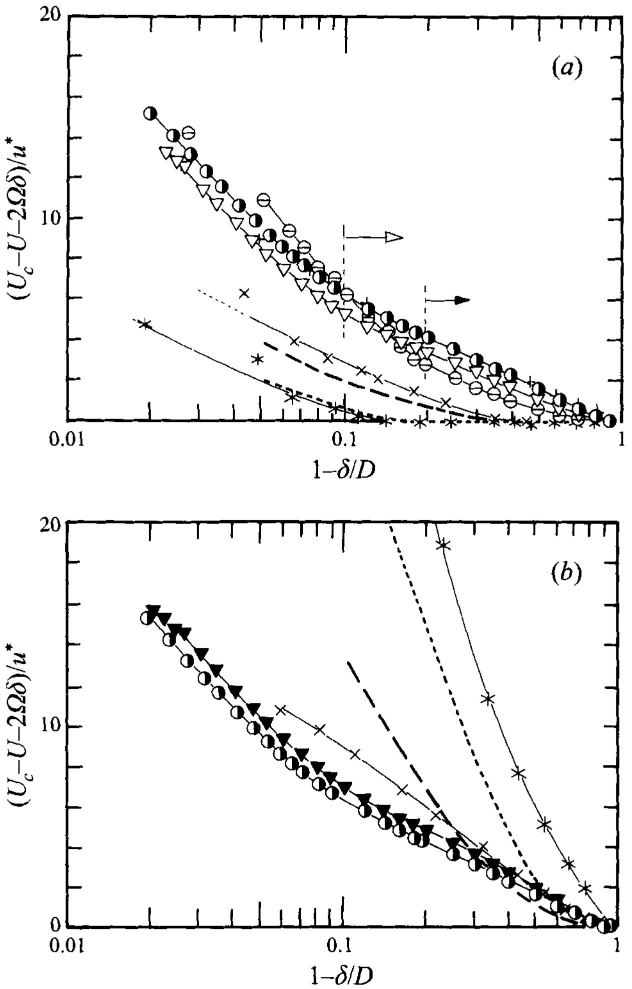

FIGURE 25. Velocity defect law. See table 1 for symbols. (*a*) Pressure side. Kristoffersen & Andersson: ---, $\Omega D/u_* = 0.95$; -------, 3.16. Johnston *et al.*: +, $\Omega D/u_* = 0$; ×, 0.55; ✳, 1.57. (*b*) Suction side. Kristoffersen & Andersson: ---, $\Omega D/u_* = -0.15$; ------, -0.5. Johnston *et al.*: ×, $\Omega D/u_* = -0.68$; ✳, -3.71.

of non-rotating flow, but their distribution depends on $\Omega D/u_*$ and *Re*. Such an *Re*-dependence may be caused by the low *Re* prevailing on the suction side.

5. Concluding remarks

Turbulent channel flows that are influenced both by the Coriolis force and low Reynolds number effects are studied. The controlling parameters are Re^* and $\Omega\nu/u_*^2$ for the wall region and $\Omega D/u_*$ and Re^* for the core region. These parameters, which are ratios among the three length scales (i.e. viscous, Coriolis and outer length scales), are sufficient to describe the flow. From the experimental data, the constants K_1, K_2 and K_3 in equation (6) are about 30–50, 0.008–0.015 and 0.2–0.3, respectively. The flow diagram shows geometrically how the flow structure changes with these parameters. The rate of change of skin friction due to the Coriolis force can be expressed as a function of $\Omega\nu/u_*^2$ except when the flow is relaminarized. On the suction side there are two cases in which the flow is relaminarized: (i) the Coriolis force stabilizing effect is responsible for it in the case $Re \geqslant 2500$; and (ii) both the Coriolis force and low Reynolds number effects are responsible for it in the case of Re less than 2500.

The law of the wall is modified by the length scales δ_c and D is $|\Omega| \nu/u_*^2$ is large and/or Re^* is small. The low Reynolds number effect affects C_1 (the additive constant of the log–law) and the Van-Driest damping factor A^+ but not κ. The Coriolis force effect alters both C_1 and κ as functions of $\Omega\nu/u_*^2$. The lower boundary of the distance from the wall beyond which the Coriolis force effects appears, $y^+_{1\%}$, depends only on $|\Omega| \nu/u_*^2$. The Coriolis region is shown to exist where the Coriolis length scale δ_c is the only scale affecting the flow and the velocity follows equation (23). The velocity defect law, modified by the Coriolis force effect, shows that on the pressure side the velocity distribution in the core region depends on $\Omega D/u_*$, and the mean absolute vorticity there is zero when $\Omega D/u_* > 1.6$.

REFERENCES

Akima, H. 1972 Interpolation and smooth curve fitting based on local procedures. Algorithm433, Comm. ACM 15, 10, 914–918.

Antonia, R. A., Teitel, M., Kim, J. & Browne, L. W. B. 1992 Low-Reynolds-number effects in a fully developed turbulent channel flow. *J. Fluid Mech.* **236**, 579–605.

Bhatia, J. H., Durst, F. & Jovanovic, J. 1982 Corrections of hot-wire anemometer measurements near walls. *J. Fluid Mech.* **122**, 411–431.

Bradshaw, P. 1969 The analogy between streamline curvature and buoyancy in turbulent shear flow. *J. Fluid Mech.* **36**, 177–191.

Clark, J. A. 1968 A study of incompressible turbulent boundary layers in channel flow. *Trans. ASME* D: *J. Basic Engng* **90**, 455–467.

Comte-Bellot, G. 1963 Turbulent flow between two parallel walls. *PhD thesis, University of Grenoble.*

Dean, R. B. 1978 Reynolds number dependence of skin friction and other bulk flow variables in two-dimensional rectangular duct flow. *Trans. ASME* I: *J. Fluids Engng* **100**, 215–223.

Huffman, G. D. & Bradshaw, P. 1972 A note on von Karman's constant in low Reynolds number turbulent flows. *J. Fluid Mech.* **53**, 45–60.

Hussain, A. K. M. F. & Reynolds, W. C. 1975 Measurements in fully developed turbulent channel flow. *Trans. ASME* I: *J. Fluids Engng* **97**, 568–580.

Jacquin, L., Leuchter, O., Cambon, C. & Mathieu, J. 1990 Homogeneous turbulence in the presence of rotation. *J. Fluid Mech.* **220**, 1–52.

Johnston, J. P., Haleen, R. M. & Lezius, D. K. 1972 Effects of spanwise rotation on the structure of two-dimensional fully developed turbulent channel flow. *J. Fluid Mech.* **56**, 533–557.

Kim, J. 1983 The effect of rotation on turbulence structure. *Proc. 4th Symp. on Turbulent Shear Flows, Karlsruhe*, pp. 6.14–6.19.

Koyama, H., Masuda, S., Ariga, I. & Watanabe, I. 1979 Stabilizing and destabilizing effects of Coriolis force on two-dimensional laminar and turbulent boundary layers. *Trans. ASME* A: *J. Engng for Power* **101**, 23–31.

Kristoffersen, R. & Andersson, H. I. 1993 Direct simulations of low Reynolds number turbulent flow in a rotating channel. *J. Fluid Mech.* **256**, 163–197.

Launder, B. E., Tselepidakis, D. P. & Younis, B. A. 1987 A second-moment closure study of rotating channel flow. *J. Fluid Mech.* **183**, 63–75.

Miyake, Y. & Kajishima, T. 1986 Numerical simulation of the effects of Coriolis force on the structure of turbulence. *Bull. JSME* **29**, 256, 3347–3351.

Moore, J. 1967 Effects of Coriolis on turbulent flow in rotating rectangular channels. *Gas Turb. Lab. Rep.* 89. MIT.

Patel, V. C. & Head, M. R. 1969 Some observations on skin friction and velocity profiles in fully developed pipe and channel flows. *J. Fluid Mech.* **38**, 181–201.

Shima, N. 1993 Prediction of turbulent boundary layers with a second-moment closure: part II – Effect of streamline curvature and spanwise rotation. *Trans. ASME* I: *J. Fluid Engng* **115**, 64–69.

So, R. M. 1975 A turbulent velocity scale for curved shear flows. *J. Fluid Mech.* **70**, 37–57.

Speziale, C. G. & Thangam, S. 1983 Numerical study of secondary flows and roll-cell instabilities in rotating channel flow. *J. Fluid Mech.* **130**, 377–395.

Watmuff, J. H., Witt, H. T. & Joubert, P. N. 1985 Developing turbulent boundary layers with system rotation. *J. Fluid Mech.* **157**, 405–448.